

Segmented plasma flow meter response from kinetic simulations

Guangdong Liu¹ and Richard Marchand¹

¹University of Alberta

November 23, 2022

Abstract

A relatively simple design of a segmented flow meter (SF meter) is presented for measuring in situ plasma flow velocities and other space plasma parameters.

The response of the flow meter to space environment is simulated for plasma conditions representative of the ionosphere at mid and low latitudes using a Particle In Cell (PIC) code.

A synthetic data set consisting of ion currents collected by several segments of the flow meter, and the physical parameters for which they were calculated, is then used to construct a solution library from which inference models can be constructed, using radial basis function (RBF) and neural network regressions.

Simulation results show that with such a flow meter, it should be possible to infer plasma flow velocities in the direction perpendicular to the ram direction, with uncertainties of 45 m/s or less.

Models can also be constructed to infer plasma densities, with a relative error of 23 %.

This work is presented as a first assessment and proof of concept for an original design of a simple and robust flow meter.

Abstract

A relatively simple design of a segmented flow meter (SF meter) is presented for measuring in situ plasma flow velocities and other space plasma parameters. The response of the flow meter to space environment is simulated for plasma conditions representative of the ionosphere at mid and low latitudes using a Particle In Cell (PIC) code. A synthetic data set consisting of ion currents collected by several segments of the flow meter, and the physical parameters for which they were calculated, is then used to construct a solution library from which inference models can be constructed, using radial basis function (RBF) and neural network regressions. Simulation results show that with such a flow meter, it should be possible to infer plasma flow velocities in the direction perpendicular to the ram direction, with uncertainties of 45 m/s or less. Models can also be constructed to infer plasma densities, with a relative error of 23 %. This work is presented as a first assessment and proof of concept for an original design of a simple and robust flow meter.

1 Introduction

Plasma winds are a key manifestation of the dynamical processes at play in the ionosphere, including ionospheric coupling with the magnetosphere and with solid Earth. This has motivated the use of various instruments mounted on satellites to measure plasma flow velocities under different space plasma environments. In addition to affecting ground infrastructures (Pirjola, 2000), events such as magnetic storms or substorms can be responsible for satellite malfunction and, in extreme cases, total loss (Baker, 2000). These storms cause turbulence in the magnetosphere, which often result in strong currents and winds. Thus monitoring ionospheric winds provides key information for a better understanding of our near-space environment, which in turn can lead to improved mitigation measures in case of extreme events. Ionospheric winds can also provide information on solid Earth activity such as earthquakes, volcanic eruptions, or high yield underground explosions (Rudenko & Uralov, 1995; Davies & Archambeau, 1998; Krasnov & Drobzheva, 2005; Parrot et al., 2006; Parrot, 2012; Yang et al., 2012; Ryu et al., 2014; Shen et al., 2018; De Santis et al., 2019). Two types of waves are being considered in relation to earthquakes. Post seismic acoustic and gravitational waves have been observed with satellites in low Earth orbit (LEO), and their connection with solid Earth phenomena is well understood from theory and computer simulations (Rudenko & Uralov, 1995; Davies & Archambeau, 1998; Krasnov & Drobzheva, 2005; Yang et al., 2012). Direct observations and statistical analyses have also been reported to support the occurrence of electromagnetic wave signatures prior to large earthquakes (Parrot et al., 2006; Parrot, 2012; Ryu et al., 2014; Shen et al., 2018; De Santis et al., 2019). While not yet demonstrated, the possibility of observing ionospheric perturbations prior to large earthquakes remains a topic of vital interest, especially in countries located in seismically active parts of the planet (ibid).

Several designs of plasma flow meters have been used on satellites to measure ionospheric winds, including retarding potential analyzers (Hanson et al., 1973; R. A. Heelis & Hanson, 2013; Satir et al., 2015), ion drift meters (Hundhausen et al., 1967; Galperin et al., 1973; Hanson et al., 1973; Galperin et al., 1974; Hanson & Heelis, 1975; R. Heelis et al., 1981; Ogilvie et al., 1995; Reigber et al., 2003; Berthelier, Godefroy, Leblanc, Seran, et al., 2006; Stoneback et al., 2012; R. A. Heelis et al., 2017), “top hat” analyzers (C. Carlson et al., 1982; C. W. Carlson & McFadden, 2013; C. W. Carlson et al., 2001), ion imagers (Whalen et al., 1994; Yau et al., 1998; Knudsen et al., 2003; Yau et al., 2015; Knudsen et al., 2017), and segmented Langmuir probes (Séran et al., 2005; Lebreton et al., 2006; Santandrea et al., 2013). The first satellites equipped with ion drift meters were deployed in the 1960s and 1970s (Hundhausen et al., 1967; Galperin et al., 1973; Hanson et al., 1973; Galperin et al., 1974; Hanson & Heelis, 1975; R. Heelis et al., 1981). While the names differed, the working principles were similar. A simplified schematic of such

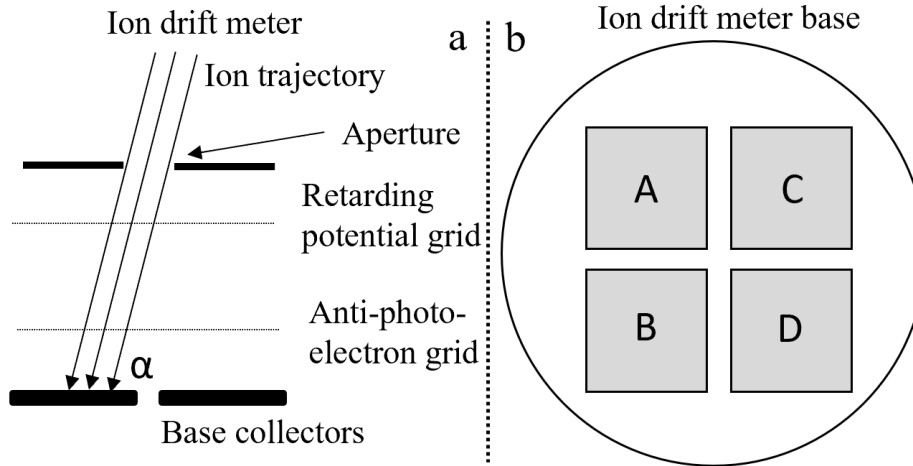


Figure 1. Illustration of an ion drift meter with integrated retarding potential analyzer. The side view in panel (a) illuminates a cross section of the aperture, grids, and collector plates. Panel (b) illustrates the four collectors at the base of the sensor.

63 a device is shown in Fig. 1. In this configuration, ions enter the sensor from the top aperture
 64 with a retarding potential analyzer from which incoming ion masses and speeds can be
 65 determined. As shown on panel (a) of the figure, the voltage applied to the top grid is
 66 swept so as to block ions with varying energies from entering the sensor. As voltage is
 67 increased, abrupt drops are measured in the collected currents (R. A. Heelis & Hanson,
 68 2013). The voltages at which these reductions occur, correspond to different energy to
 69 charge ratios of incoming ions, in the satellite reference frame. The magnitude and shape
 70 of these drops also provide information on ion temperatures and relative densities. The
 71 second grid is biased to a fixed negative voltage to prevent the escape of photoelectrons
 72 from the base collectors. When collectors are exposed to UV radiation, simulations suggest
 73 that most photoelectrons are reflected back to the collector from which they were
 74 emitted (Stoneback et al., 2012). The angle of incidence α of the plasma flow is deter-
 75 mined from the relative currents collected by the segments. This, combined with the ram
 76 speed measured with the retarding potential analyzer, is used to determine the trans-
 77 verse flow velocity. The retarding potential analyzer/ion drift meter is robust, and it was
 78 used in many space missions. For example, VEIS on the WIND spacecraft was used to
 79 study the foreshock subsonic particles reflected from the bow shock (Ogilvie et al., 1995).
 80 This instrument can also be used to measure electron energies by reversing the analyzer
 81 electric field polarization. Similarly, IAP on DEMETER was used to measure plasma
 82 flow velocities with particular attention to the perturbed flow induced by waves caused
 83 by seismic activity (Berthelier, Godefroy, Leblanc, Seran, et al., 2006). The accuracy of
 84 ram speed measurements, obtained with IAP on DEMETER, was estimated to be ap-
 85 proximately 10%, based on laboratory calibrations and computer simulations (Séran, 2003;
 86 Berthelier, Godefroy, Leblanc, Seran, et al., 2006). Similar flow meters are also used on
 87 spacecraft, such as Dynamics Explorer B (R. Heelis et al., 1981), C/NOFS satellite (Stoneback
 88 et al., 2012), and Ionospheric Connections Explorer (R. A. Heelis et al., 2017). A sim-
 89 ilar instrument has been developed based on the same basic principle, referred to as the
 90 "backplane design". In this configuration, ions travel to the base of the sensor and are
 91 deflected by a strong electric field, to be collected on the backside of collector seg-
 92 ments, as illustrated in Fig. 2. This configuration was used in DIDM on the CHAMP satellite
 93 to prevent direct UV radiation from entering the collectors, and minimize perturbations
 94 from photoelectrons (Reigber et al., 2003).
 95

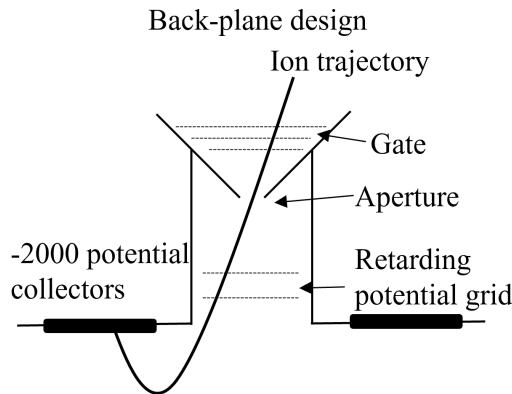


Figure 2. DIDM on the CHAMP satellite uses a back-plane design of ion drift meter. Ions are deflected 180° once they are in the detector dome using a -2000 volts potential.

96 The “top-hat” analyzer shown in panel a of Fig. 3 is widely used to sample charged
 97 particles over 360° in azimuthal (C. Carlson et al., 1982; C. W. Carlson & McFadden,
 98 2013; C. W. Carlson et al., 2001). Trajectories of incoming particles are bent by a ra-
 99 dial electric field between two hemispherical electrodes of different radii. For a given po-
 100 tential difference between the two hemispheres, only particles in a narrow range of en-
 101 ergy to charge ratio can follow a trajectory leading to the base collectors. The energy
 102 spectrum of the particles is then obtained by sweeping the potential difference between
 103 the two analyzer hemispheres. The “top hat” analyzer provides a pitch-angle range over
 104 the full 2-dimensional plane through the analyzer aperture. Ion imagers are yet another
 105 type of flow meter in which, as illustrated in panel b of Fig. 3. In this configuration, ions
 106 enter through an aperture, and are dispersed by an electric field between two concen-
 107 tric hemispherical shields, onto a detector array, as determined by their energy to charge
 108 ratio. Depending on the setup, incoming particle velocities are measured over 180°, or
 109 the full 360° degrees in azimuthal angles. For example, the F3C Cold Plasma Analyzer
 110 (CPA) instrument on Freja can sample ions over a range of 360° in azimuthal angles around
 111 the satellite (Whalen et al., 1994). On Swarm, the Electric Field Instrument (EFI) con-
 112 sists of two imagers, each with 180° wide apertures, oriented perpendicularly to one an-
 113 other, thus providing a three-dimensional sample of incoming ion distributions (Knudsen
 114 et al., 2017). Other spacecraft are also equipped with ion imagers, including ePOP (Yau
 115 et al., 2015), and Plante-B (Yau et al., 1998). In principle, ion imagers can accurately
 116 measure ion drift velocities and ion masses without the need for sweeping voltage. The
 117 accuracy with which plasma flow velocity can be inferred with ion imagers has been as-
 118 sessed to be of order 20 m/s based on rocket-based measurements (Sangalli et al., 2009).
 119 In space, performance can vary due to several factors, including satellite potentials, chang-
 120 ing plasma conditions, and aging of sensor components (Marchand et al., 2010; Knud-
 121 sen et al., 2017).

122 Segmented Spherical Langmuir Probes have also been used to measure bulk plasma
 123 flow. The surface of the probe is divided into several equipotential spherical caps or seg-
 124 ments facing different directions, from which individual currents are measured. The rela-
 125 tive currents from these segments and the supporting sphere can in principle be used
 126 to infer plasma density, temperature, and plasma flow velocity (Lebreton et al., 2006).
 127 This instrument was used on satellites such as DEMETER and Proba-2 (Séran et al.,
 128 2005; Lebreton et al., 2006; Santandrea et al., 2013). It is also possible to infer plasma
 129 flow velocities indirectly from measured electric fields and the relation for the $\vec{E} \times \vec{B}$
 130 drift. Boom-supported electric field probes are used on numerous satellite and rocket ex-
 131 periments, including ICE on DEMETER (Berthelier, Godefroy, Leblanc, Malingre, et

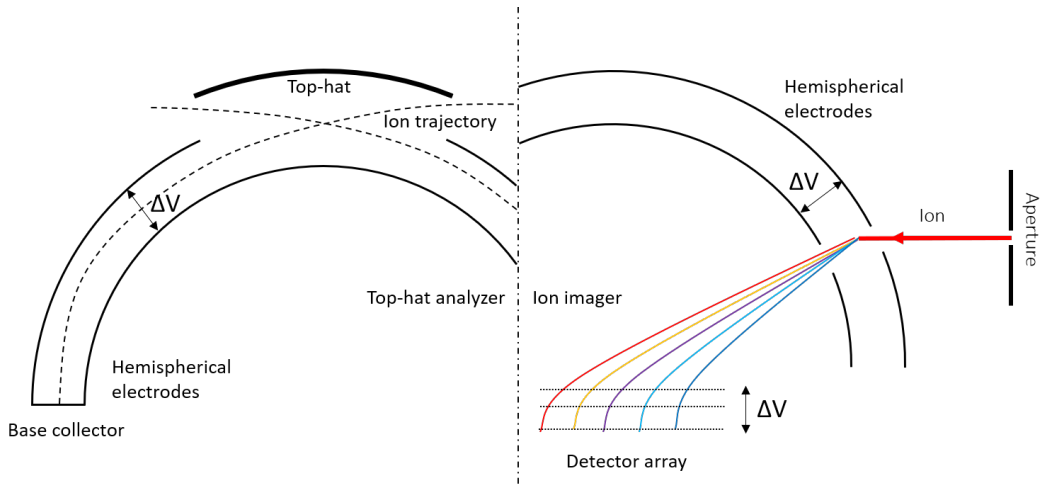


Figure 3. Illustration of a ‘top hat’ analyzer and ion imager. Both devices can sample ions over 360° azimuthal angles.

132 al., 2006) and the Fields Instrument on FAST (Ergun et al., 2001). At lower latitudes,
 133 it is also possible to measure the neural wind speed in the ram direction, from the Doppler
 134 shift in atmospheric emission lines using an interferometer with laser beams (Englert et
 135 al., 2007).

136 One important difference between flow meters and more familiar Langmuir probes
 137 is that several theories have been developed to interpret measurements made with the
 138 latter, while no theory exists for the former. As a result, the inference of plasma flow ve-
 139 locities from flow meters must rely on laboratory calibration and computer simulations.
 140 Thus the goals of this study are to i) characterize the response of a proposed simple flow
 141 meter applicable to ionospheric wind, using computer simulations, ii) construct inference
 142 models based on multivariate regression, and iii), assess their predictive skills for con-
 143 ditions representative of the lower ionosphere. In the remainder of this paper, we present
 144 the geometry of a plasma flow meter, which should combine simplicity, robustness, and
 145 accuracy. The performance of the proposed instrument is assessed based on a combina-
 146 tion of synthetic data constructed with computer simulations, and multivariate regres-
 147 sions. The simulation techniques, the sensor geometry, and the regression approaches are
 148 presented in Section 2. Simulation results and assessments of inference skills are presented
 149 in Section 3. The final section summarizes our findings and contains some concluding
 150 remarks.

151 2 Methodology

152 The flow meter geometry considered is shown in Fig. 4. It is sufficiently compact
 153 to be mounted on small satellites such as CubeSats. In the satellite reference frame, ions
 154 are incident from the ram direction, with speeds approximately equal to the satellite or-
 155 bital speed. Thus, the meter needs to be mounted on the ram face of the satellite to al-
 156 low ions to enter the aperture. In the proposed design, there are a total of 19 collect-
 157 ing segments, from which individual currents are measured. The top ring aperture is bi-
 158 ased to -4 V with respect to the spacecraft in order to repel electrons and attract ions
 159 into the cone. This negative voltage at the top also serves to increase the radial disper-
 160 sion of entering ions. All other segments at the base are biased to $+3$ V in order to i)
 161 enhance dispersion of the ion beam penetrating the sensor, and ii) retain photoelectrons
 162 that might be emitted, should solar UV enter the cavity. Enhancing radial spread of the
 163 incident ion beam at the base should make the distribution of collected currents more

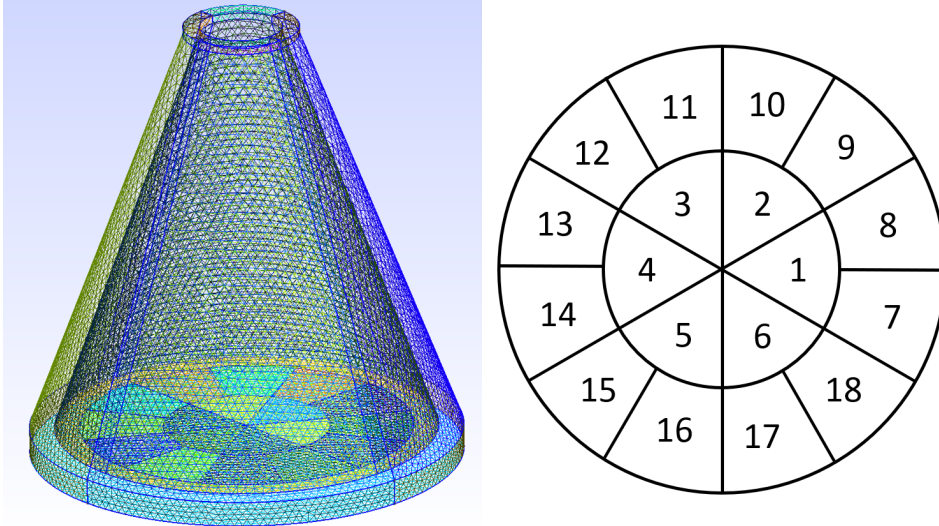


Figure 4. Illustration of the 3D geometry of the SF meter (left), and the 18 sectors at the base (right). The conical shell has a height of 5 cm, the outer radius at the base is 2.3 cm, and that at the top ring is 0.7 cm.

164 sensitive to the ion mass distributions and hence, to the ion effective mass. The curved
 165 conical faces of the sensor, both inside and outside, are assumed to be grounded to the
 166 satellite bus, implying that they would also be at the satellite potential V_s with respect
 167 to background plasma. Simulations indicate that if the satellite potential V_s is positive
 168 and larger than ~ 1 V, the base sensors start collecting a noticeable amount of electrons
 169 passing through the top aperture, which in turn would interfere with the measurement.
 170 In the lower ionosphere at mid and low latitudes where photoelectron and secondary elec-
 171 tron emission are not significant, a spacecraft should be charged negatively. In the fol-
 172 lowing, the proposed sensor response is assessed assuming spacecraft potentials ranging
 173 from -2 to 1 V. The following paragraphs describe the approaches used to characterize
 174 the response of the flow meter to diverse space environment conditions, to construct mod-
 175 els to infer physical parameters of interest from measurements, and to assess their pre-
 176 dictive skills.

177 2.1 Symmetry

178 One key feature of the device considered is symmetry. In order to characterize the
 179 response of the multiple sensors to flows with components transverse to the cone axis,
 180 we need to carry out many three-dimensional kinetic simulations assuming different plasma
 181 parameters, consisting of densities, temperatures, ion compositions, flow velocities, and
 182 satellite potentials. These simulations are used to construct a solution library consist-
 183 ing of collected currents by each of the 19 segments, with corresponding space-plasma
 184 conditions. Without symmetry, simulations would be required for transverse flows cov-
 185 ering the full 360° around the sensor axis. With the six-fold rotational symmetry, and
 186 the mirror symmetry in the 18 collecting segments at the base of the sensor seen in Fig.
 187 4, however, simulations are only needed in a much smaller 30° angular sector. For ex-
 188 ample, simulations can be carried out to calculate currents collected by all segments, for
 189 flow velocities with transverse velocities in only the 30° sector 8. These currents can then
 190 be mirror imaged with respect to the horizontal axis between sectors 7 and 8 (or 13 and
 191 14), to extend results to transverse velocities directed in sector 7. From there, the six-
 192 fold rotational symmetry can be used to further extend our simulation results to trans-

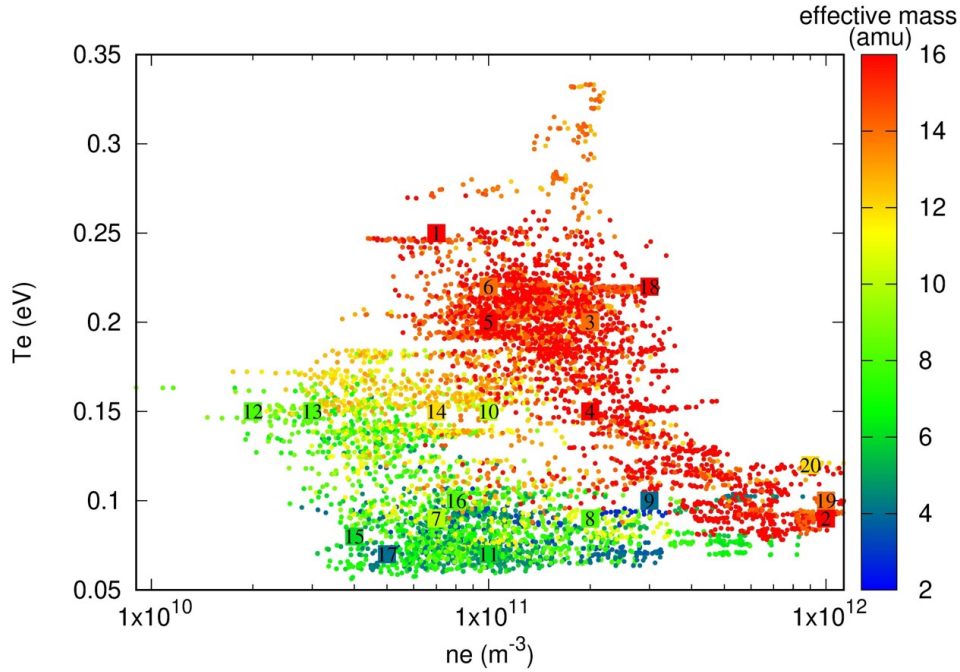


Figure 5. Scatter plot of plasma parameters obtained from the IRI model, corresponding to different latitudes, longitudes, altitudes, and times, as listed in Table 1. Numbered squares identify parameters used in the kinetic simulations.

193 verse velocities in all sectors, covering the full 360° of azimuthal angles; thus reducing
 194 the number of simulations by a factor 12 compared to what would be needed in the ab-
 195 sence of symmetry.

196 2.2 Kinetic Simulations

197 The response of the sensor to different ionospheric wind conditions is simulated us-
 198 ing the three-dimensional PIC code PTetra (Marchand, 2012; Marchand & Resendiz Lira,
 199 2017). In this model, space is discretized with unstructured adaptive tetrahedral meshes
 200 (Frey & George, 2007; Geuzaine & Remacle, 2009), and Poisson's equation is solved at
 201 each time step, using Saad's GMRES sparse matrix solver (Saad, 2003). Electrons and
 202 ions are treated kinetically, accounting for their physical masses, and particle trajecto-
 203 ries are calculated self-consistently using computed electric fields. The parameters as-
 204 sumed in the simulations have been selected so as to be representative of ionospheric con-
 205 ditions encountered by satellites in low Earth orbit (LEO) at mid, and low latitudes. A
 206 sample of electron and ion temperatures, electron densities, and ion mass distributions
 207 was obtained from the International Reference Ionosphere (IRI) (Bilitza et al., 2014) model
 208 for different latitudes, longitudes, altitudes, and times. The result is shown in Fig. 5, with
 209 points in the density-temperature scatter plot, and colors indicating ion effective masses.
 210 The numbered squares in the figures identify the twenty sets of plasma parameters $(T_e, T_i, n_e, m_{i_{eff}})$
 211 for which simulations were made. For each of the selected set of plasma parameters, sev-
 212 eral simulations were made for different satellite potentials, incoming plasma ram speeds,
 213 and transverse velocities distributed in the 30° sector 7, for a total of 310 simulations.
 214 When extended to the full 360° circle as described above, this produces a solution library
 215 consisting of 2676 entries used to train and assess our inference models.

216 For simplicity, and considering that in the conditions considered, O^+ and H^+ con-
 217 stituted 94% or more of all ion species, only these two ion species were considered in the

Table 1. Range of ionospheric conditions considered with the IRI model, and corresponding ranges in space plasma parameters.

Environment and plasma conditions	Parameter range
Years	1998 2001 2004 2009
Date	Jan 4 Apr 4 Jul 4 Oct 4
Latitude	-65° - $+65^\circ$ with increment of 26°
Longitude	0° - -360° with increment of 30°
Hours	0-24 with increment of 8 hours
Height	450-550 km
Ion temperature	0.07-0.12 eV
Electron temperature	0.09-0.25 eV
Effective ion mass	4-16 amu
Density	$2 \times 10^{10} - 1 \times 10^{12} \text{m}^{-3}$
Ram velocity	7000 -8000 m/s
Transverse speed	0-500 m/s
Angles	$0-30^\circ$
Spacecraft potential	-2-1 eV

218 simulations. Earth magnetic field is not accounted for in the simulations, owing to the
 219 fact that typical ion gyroradii in the ionosphere are of order 1 m for H^+ , and 4 m for
 220 O^+ , which are much larger than the ~ 5 cm size of the sensor considered. Secondary
 221 electron emission is ignored in the calculations because of the low electron temperatures
 222 (below 0.5 eV) encountered in the regions of interest. Photoelectron emission is also not
 223 taken into account, which is justified when the satellite is on the night side of its orbit
 224 or when the meter aperture is not exposed to solar illumination.

225 2.3 Multivariate regression

226 Given a solution library, the next step is to construct models capable of inferring
 227 plasma parameters from measurements. In the following, we describe two approaches for
 228 constructing such models, which will be applied and assessed for their inference skills in
 229 Sec. 3. Several approaches are possible, including empirical parametric fits and multi-
 230 variate regressions. Here we use two regression approaches based on i) Radial Basis Func-
 231 tions (RBF), and ii) Deep Learning Neural Networks. In either case, two steps are in-
 232 volved in the construction of a model. The first step consists of training a model on a
 233 subset of the solution library; the “training set”, while the second step consists of ap-
 234 plying the trained model to a distinct data set; the validation set, consisting of the re-
 235 maining subset of the library. The inference skill of the model is generally better on the
 236 training than on the validation set. Model skills applied to the training set can be im-
 237 proved by further refining the model, but improvements in training do not necessarily
 238 correspond to improvements in validation inferences. Beyond a certain level of refine-
 239 ment in training, “overfitting” occurs, and inference skill degrades for the validation set.
 240 A good model is one with the right level of refinement so as to provide the best infer-
 241 ence skill when applied to the validation set. Let us now briefly present the two regres-
 242 sion methods used in our study.

243

2.3.1 Radial Basis function

244

245

246

247

Radial basis Function is one of the most basic regression techniques, and it is applied in many fields, including image mapping, and data tracking (Buhmann, 2003). Given a set of independent vectors \vec{X} and corresponding dependent vectors \vec{Y} , a general expression for RBF regression is given by

$$\vec{Y} = \sum_{i=1}^n a_i G \left(\left| \vec{X} - \vec{X}_i \right| \right), \quad (1)$$

248

249

250

251

252

253

254

255

256

257

258

259

260

261

262

263

264

where \vec{Y} is a vector of parameters to be inferred, \vec{X} is a vector consisting of independent, measured quantities, and (\vec{X}_i, \vec{Y}_i) are reference nodes or pivots in the space of independent-dependent variables. G is a function of a real variable, a_i are fitting coefficients, and n is the number of pivots used in the regression. In RBF, \vec{X} and \vec{Y} can be vectors of different dimensions. In what follows, however, dependent variables \vec{Y} will always be scalars (vectors of dimension one), and \vec{X} will be vectors of different dimensions, depending on the physical parameter being inferred. In Eq. 1, the argument of G is the L^2 norm, or Euclidean distance between \vec{X} and \vec{X}_i ; whence the name “radial” in RBF. The choice of G is arbitrary, provided that, for a given set of pivots, the set of n interpolating functions in Eq. 1 be independent of one another. When constructing a regression model with RBF, the function G , and the number and distribution of pivots must be chosen so as to yield the best possible predictive skill for a given problem. Two G functions have been found to give good predictive skill for the inferred physical parameters considered. They are described with the physical parameters in Sec. 3. The number and distribution of pivots have similarly been selected so as to provide optimal accuracy when inferring dependent parameters in a validation set. Two types of cost functions have been considered, the maximum absolute error (MAE):

$$\epsilon_{abs} = \text{Max} | Y_{sim} - Y_{mod} |, \quad (2)$$

265

and the maximum relative error (MRE):

$$\epsilon_{rel} = \text{Max} \left| \frac{Y_{sim} - Y_{mod}}{Y_{mod}} \right|, \quad (3)$$

266

267

calculated over a given data set, where Y_{sim} are known plasma parameters used in the simulation such as density, and Y_{mod} are the model-inferred parameters.

268

269

270

In order to carry out this task and construct a model, the fitting coefficients a_i in Eq. 1 have to be determined. This is done first by requiring collocation of inferred and known parameters at pivots; that is, by solving the set of equations

$$\sum_{j=1}^N a_j G(|\vec{X}_i - \vec{X}_j|) = \vec{Y}_{i,sim}, \quad i = 1, N. \quad (4)$$

271

272

273

274

275

276

277

278

279

280

281

282

283

284

285

Given a training data set of \mathcal{N} nodes, the selection of N pivots is made by constructing models for all possible \mathcal{N} choose N combinations of pivots among the \mathcal{N} nodes, and selecting the one which minimizes the cost function. When the best distribution of pivots is found, the model can be further improved by relaxing collocation, by allowing for small deviations from the $\vec{Y}_{i,sim}$ and minimizing the cost functions with respect to these deviations. Yet another improvement is to go over all \mathcal{N} choose N possible combinations of pivots in parallel on n multiple processors, in such a way that each processor goes through different combinations. In this case, each processor finds its unique best combination of pivots. One obvious advantage of this is an increase in speed. Another one is that relaxation, or accounting for the “nugget effect”, can be applied to each of the distinct n best combinations, and selecting the combination which, after relaxation, produces the smallest cost function. It is found that the best combination then, is not necessarily the one that minimizes the cost function before relaxation. With this strategy, and using several processors, it is possible to reduce the cost function in a training set by several %, compared to a minimization made without relaxation.

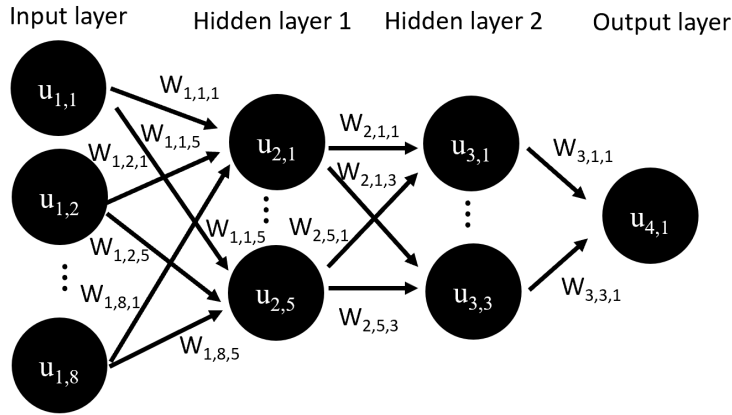


Figure 6. Schematic of a feedforward neural network.

286 Given the size of the data, \mathcal{N} choose N can be very large. One strategy is to com-
 287 bine RBF with the Monte Carlo method to do a non-exhaustive search for the model.
 288 In this approach, a small subset (e.g. 100 entries) is picked each time randomly from the
 289 training data set to train a model, then the model is applied to the entire training data
 290 set to calculate the cost function. The best model is selected after a certain time and
 291 it is applied to the validation data set to determine the validation error.

292 **2.3.2 Neural network**

293 Neural networks have increasingly been proven useful in many applications, includ-
 294 ing plasma physics and space physics (Barkhatov & Revunov, 2010; Breuillard et al., 2020).
 295 In this work, we use the feedforward deep learning networks to infer plasma parameters
 296 from currents collected from the 19 segments in the proposed flow meter. An illustra-
 297 tion of a feedforward network is shown in Fig. 6, with the input layer, hidden layers, and
 298 the output layer. In our problem, each node in the input layer is assigned a current from
 299 one of the segments. Node j in layer i is assigned a value $u_{i,j}$, and each node of the next
 300 layer $i + 1$ is “fed” by all the nodes of the previous layer according to

$$u_{i+1,k} = \sum_{j=1}^{n_i} w_{i,j,k} f(u_{i,j} + b_{i,j}), \quad (5)$$

301 where $w_{i,j,k}$ are weight factors, $b_{i,j}$ are bias terms, and f is a nonlinear activation func-
 302 tion. In this study, the bias terms are all set to zero. The w coefficients are first gener-
 303 ated using the Monte Carlo method, and then gradient descent is used to further decrease
 304 the cost function over the training data. Training sets consisting of 500 data entries are
 305 used to train neural network models. As with RBF, many models are trained before the
 306 final model is selected. The models are then applied to the validation data sets to ob-
 307 tain the validation error.

308 **2.4 Noise**

309 Given a trained model, the skill and robustness of inference are tested against noise
 310 in the validation sets. Noise in collected currents can be statistical in nature, or it can
 311 be associates with physical processes such as waves and turbulence. The current collected
 312 by a segment is given by the number of particles N collected in a given sampling time
 313 τ , multiplied by their respective charges, and divided by τ ; that is, assuming singly ion-

314 ized ions for simplicity,

$$I = \frac{Ne}{\tau}. \quad (6)$$

315 Owing to the discrete nature of this process, the number N follows approximately Pois-
 316 son statistics. The standard deviation; that is, the noise level, in N is therefore approx-
 317 imately the square root of \bar{N} , the average value of N : $\sigma_N \simeq \sqrt{\bar{N}}$. Thus, it follows that
 318 the standard deviation in the collected current is approximately

$$\sigma_I \simeq \frac{\sigma_N e}{\tau} \simeq \sqrt{\frac{Ie}{\tau}}. \quad (7)$$

319 In simulations however, the number of simulation particles N_s accounted for, is gener-
 320 ally smaller than the actual number of physical particles in a plasma. In order to account
 321 for that, simulation particles carry a statistical weight w , corresponding to the number
 322 of actual particles that they “represent”. Currents calculated in simulations are there-
 323 fore obtained by multiplying the charge of each collected particle by its statistical weight
 324 as in

$$I = \frac{wN_s e}{\tau}, \quad (8)$$

325 and the resulting standard deviation in the current calculated in a simulation is

$$\sigma_I \simeq \frac{w\sigma_N e}{\tau} \simeq \sqrt{\frac{wIe}{\tau}}. \quad (9)$$

326 The standard deviation in the collected current can also be calculated directly from our
 327 simulation results, by considering a case with zero transverse flow velocity. In this case,
 328 by symmetry, all six inner segments should collect the same current, as should the twelve
 329 outer segments. Thus, calculating the standard deviation in these currents provides an
 330 estimate of the intrinsic statistical noise in the current collected by a single segment. For
 331 example, in one of the simulations, using a sampling time of $1\mu\text{s}$, in which ions have a
 332 statistical weight $w = 2$, the average current per inner segment is calculated to be $I \simeq$
 333 $2n\text{A}$. In this case, the standard deviation of the current over the six segments is found
 334 to be $\simeq 29\text{pA}$, which is in good agreement with the 25pA estimated from Eq. 9.

335 In order to test the robustness of our models, additional noise is introduced in our
 336 validation sets, in addition to the intrinsic statistical noise mentioned above. Here again,
 337 this added noise is assumed to be proportional to the square root of the collected cur-
 338 rent as per

$$I_\sigma = I_0 \left(1 + r\sigma \sqrt{\frac{I_0}{1n\text{A}}} \right), \quad (10)$$

339 where I_σ is the current collected with added noise, I_0 is the simulated collected current
 340 from the solution library for a given segment, σ is a relative standard deviation, and r
 341 is a zero-mean random number with Gaussian distribution and unit standard deviation.
 342 For each value of σ , 100 sets of random noise have been used to calculate the averages
 343 of the maximum errors and Root-Mean-Squared (RMS) errors reported in Tables 3.

344 **3 Results and discussion**

345 We now proceed with the construction of models for selected plasma parameters.

346 **3.1 Transverse flow velocity**

347 The inference of transverse velocities relies on the symmetry and the currents col-
 348 lected by the base 18 segments as described above. This is made in two steps in which
 349 i) the direction of the transverse flow velocity, and ii) its magnitude are determined.

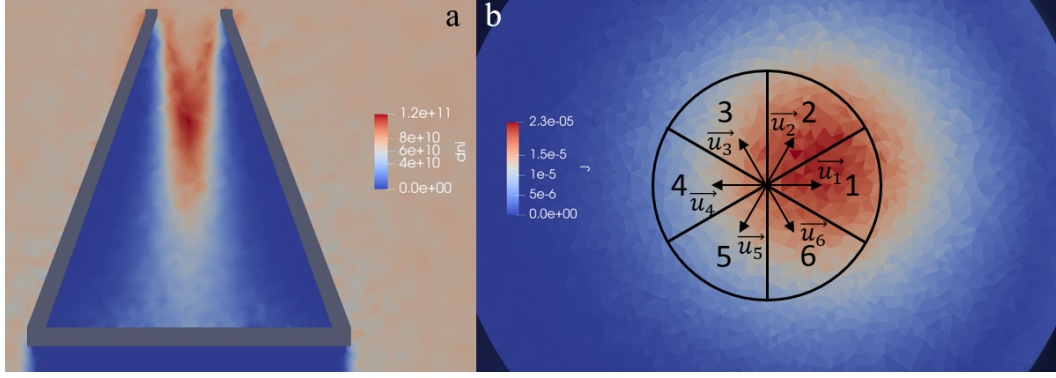


Figure 7. Cross section of the ion density in and out of the SF meter (a), and collected current density profile at the base (b). The density is in units of m^{-3} , and current density in units of Am^{-2} . This corresponds to condition 14 in Fig. 5, with n_e , $m_{i\text{eff}}$, T_e , T_i being $7 \times 10^{10} \text{ m}^{-3}$, 12 amu, 0.15 eV and 0.11 eV respectively.

Table 2. Examples of transverse wind angles obtained from \vec{U} in the vector approach. Each run number corresponding to a set of plasma conditions mentioned in section 2.2. “Simulation”, “Inner”, and “Outer” corresponding to the inner ring vector, outer ring vector and the wind direction used in the simulation.

Plasma condition#	Wind speed (m/s)	Simulation	Inner	Outer
1	125	10°	18.8°	17.6°
1	250	10°	12.2°	13.0°
1	375	10°	12.4°	12.2°
1	500	10°	10.5°	11.9°
2	125	20°	28.4°	30.8°
2	250	20°	23.7°	23.6°
2	375	20°	23.3°	23.0°
2	500	20°	21.0°	22.8°

350

3.1.1 Transverse flow direction - The vector approach

351

352

353

354

355

356

357

An obvious manifestation of a transverse flow velocity in incident plasma is an azimuthal asymmetry in the currents collected at the base of the sensor, as shown in Fig. 7. Given the geometry of the sensor, the shift in the centroid of the collected current must be in the direction of the transverse plasma flow velocity. This shift in turn can be determined from the average of the unit vector pointing in the middle of each sector, as shown in panel b of Fig. 7, weighted with the current that it collects. In practice, two averages are made, for the inner sectors as

$$\vec{U}_1 = \sum_{i=1}^6 \vec{u}_i \cdot I_i, \quad (11)$$

358

359

360

and a similar expression is used for \vec{U}_2 , calculated with the 12 outer sectors. The direction of the two vectors give indications of directions of the wind, as shown in Table 2. These vectors are then combined linearly as:

$$\vec{U} = (1 - \alpha)\vec{U}_1 + \alpha\vec{U}_2, \quad (12)$$

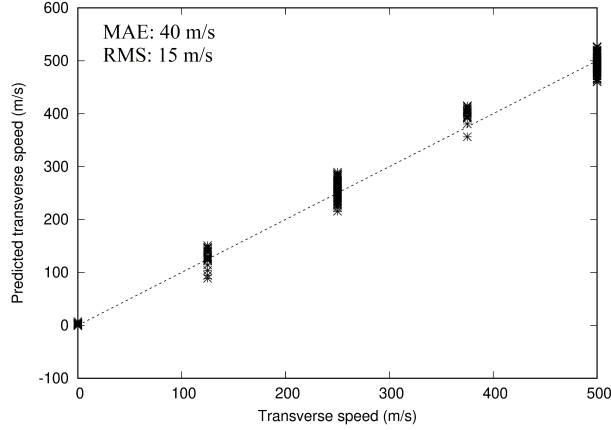


Figure 8. Correlation plot of the transverse wind speeds inferred for the validation set, vs. actual speeds used in the simulations. For reference, the dotted line corresponds to a perfect correlation. In this case, RBF is used with 5 pivots, leading to a maximum absolute error (MAE) of 40 m/s, and a RMS error of 15 m/s.

Table 3. Errors in inferred angles, transverse speeds, velocities, and densities calculated without, and with noise added to currents in the validation set.

Parameter:	Angle (°)	Speed (m/s)	Velocity (m/s)	Density (%)
Method:	Vector	RBF	Vector+RBF	RBF
Skill metric:	RMS	RMS	RMS	RMSrE
$\sigma = 0$	3.2	15	20	11
$\sigma = 1\%$	3.6	16	20	12
$\sigma = 2\%$	4.2	17	21	12
Skill metric:	MAE	MAE	MAE	MRE
$\sigma = 0$	10.7	40	45	23
$\sigma = 1\%$	15	52	58	32
$\sigma = 2\%$	20	70	75	49

361 where the parameter α is selected so as to minimize the absolute error in the inferred
 362 transverse velocity over a given training data set. $\alpha \simeq 0.94$ is found to be optimal in
 363 all cases considered, and it is the value used in the inference models considered below.

364 **3.1.2 Transverse flow speed and velocity**

365 Given a direction of the flow from Eq. 12, the transverse velocity can then be ob-
 366 tained from the transverse speed. The speed is inferred using RBF regression, in which
 367 the magnitudes of \vec{U}_1 and \vec{U}_2 are used as the two components of independent vectors \vec{X} .
 368 For example, a correlation plot of inferred speeds as a function of the actual speed from
 369 the solution library is shown in Fig. 8. In this case, the model is constructed on a train-
 370 ing set of 1338 randomly selected nodes from the solution library, using five pivots as ex-
 371 plained in Sec. 2.3.1, and it is applied to a validation set consisting of the 1338 remain-
 372 ing nodes. The regression function used here is $G(x) = 0.5x^{1.6} \times \log(x^2)$ for $x > 0$ and
 373 the cost function is the maximum absolute error over the set considered. The figure also
 374 shows the value of the cost function (40 m/s) and the RMS error (15 m/s) computed on

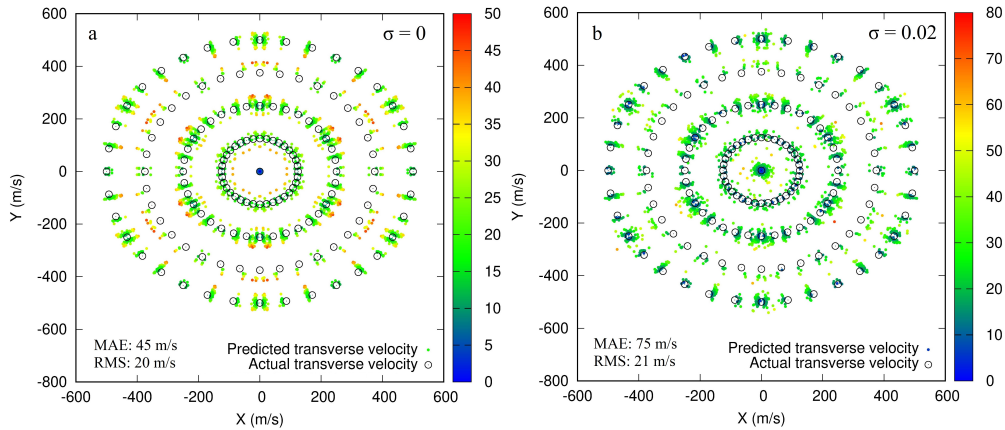


Figure 9. Actual and inferred transverse velocities without (a) and with (b) 2% added noise in the validation data set. The color scale shows the absolute errors in the model velocity predictions. Inferred velocities were obtained with RBF regression, using 5 pivots.

375 the validation set. Figure 9 shows RBF predicted transverse predicted and actual transverse
 376 transverse flow velocities without (left) and with (right) 2% ($\sigma = 0.02$) added statistical noise
 377 in the validation set using Eq. 10. Here the model uses the same training and valida-
 378 tion sets as for Fig. 8. When the model is applied to the validation set, the maximum
 379 absolute error, and root-mean-squared error are 45 m/s and 20 m/s respectively, when
 380 no noise is added. These errors increase respectively to 75 m/s, and 21 m/s when 2%
 381 relative noise is added to the validation set, which corresponds to approximately 72%
 382 of the simulation statistical noise estimated from Eq. 9. Results from neural network,
 383 not shown here, are comparable within 30%, with RBF prediction being slightly more
 384 accurate. More inference skill metrics are listed in Table 3, for different levels of added
 385 noise. As expected, our model predictive skill decreases as noise is added, and the max-
 386 imum absolute error is found to increase by a factor two for a level of added noise of ap-
 387 proximately 2%.

388 3.2 Density Prediction

389 While our primary objective is to infer ionospheric plasma flow velocities, it is inter-
 390 esting to explore the possibility for the proposed instrument to be used to infer other
 391 physical quantities. This is motivated by the fact that the currents collected by the many
 392 segments in the meter, and their relative values, are sensitive to several satellite plasma
 393 environment parameters, including ion densities and masses, ion temperatures, ram, and
 394 transverse velocities, and satellite potentials. Models were constructed for the plasma
 395 density using both RBF and neural network regression, and both are found to yield in-
 396 ferences with comparable skills. Here, however, considering the nearly two orders of mag-
 397 nitude range over which densities vary in our solution library and the fact that the den-
 398 sity is a positive definite quantity, the cost function chosen in the construction of the mod-
 399 els consists of the maximum relative error (in absolute value) over the training data set.
 400 This is preferred to the absolute error because, with the latter, models can be constructed
 401 with excellent skills for the larger densities, but poor ones for lower densities. Among
 402 the several G functions tested, the best one for predicting density was $g(\mathbf{x}) = \mathbf{x}^5$. Here,
 403 5 pivots were used as a good balance between training and validation inference skills. 500
 404 entries were used to train models using neural networks, with a four-layer network with
 405 19, 15, 7, and 1 nodes. Figure 10 shows correlation plots of inferred density, as a func-
 406 tion of actual densities obtained with neural network (left) and RBF (right) regression,

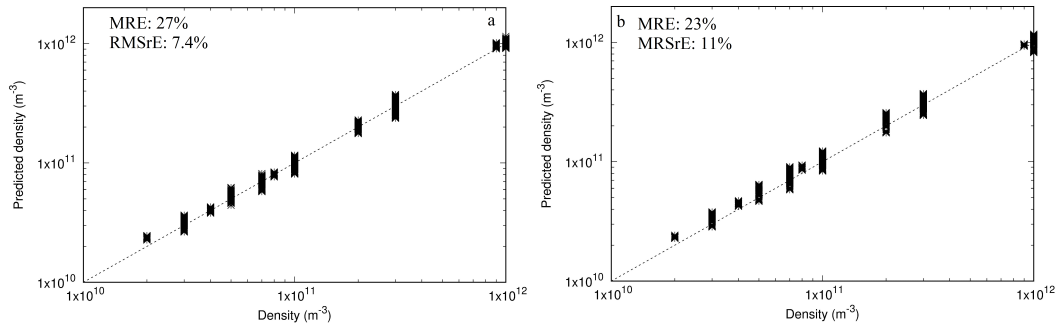


Figure 10. Predicted densities vs. densities used in simulation obtained by minimizing the maximum relative error. The neural network prediction with 500 points is shown on the left (relative error 27%) and the RBF predicted density using 5 pivots is shown on the right (relative error 23%). The dotted line corresponds to a perfect correlation between predictions and actual densities.

407 for the validation set without the addition of statistical noise. Both regression techniques
 408 yield comparable predictive skills, with maximum relative errors of 27% and 23%, and
 409 root-mean-square relative errors of 7.4% and 11% respectively for the neural network and
 410 RBF. As for the transverse flow velocity, the models' robustness to statistical noise was
 411 assessed by adding random noise to the currents collected by each segment, as per Eq.
 412 10. The impact on predictive skills is given in Table 3, which again shows a degradation
 413 of skill with an increase in the level of noise.

414 4 Summary and conclusion

415 Results are presented for a particle sensor, which could be mounted on satellites,
 416 to infer in situ transverse plasma flow velocities. The device consists of several electri-
 417 cally biased segments at the base of a conical enclosure, and a circular ring on the top
 418 aperture, from which currents are measured. Three-dimensional kinetic particle in cell
 419 (PIC) simulations are made to construct a solution library and data sets, for plasma en-
 420 vironment conditions of relevance to satellites in low Earth orbit. The symmetry of the
 421 device enables the construction of data sets for transverse velocities directed in the full
 422 360° in the plane perpendicular to the ram direction of plasma flow velocities, from sim-
 423 ulations made in only a 30° sector. Owing to the large computational resources required
 424 to carry out kinetic simulations, symmetry is key in reducing the required number of sim-
 425 ulations. Training and validation data sets, constructed with our solution library, are used
 426 to construct regression models capable of inferring transverse velocities and plasma den-
 427 sities. Two approaches are assessed for constructing such models, consisting of radial ba-
 428 sis function, and neural network regressions. The two approaches are found to have com-
 429 parable skills for inferring both transverse velocities, and plasma densities. With the con-
 430 figuration considered, it was not possible to make an accurate inference of the plasma
 431 flow speed in the ram direction, because variations in that speed have a similar effect to
 432 variations in the plasma density. Better inference of the ram speed should nonetheless
 433 be achievable by using a separate, or integrated retarding potential analyzer as illustrated
 434 in Fig. 1.

435 The level of statistical noise in the collected currents, associated with the discrete
 436 nature of kinetic simulations, explains in part the relatively small discrepancies between
 437 our model predictions and actual values in the data sets. Considering that simulations
 438 are made with significantly fewer particles than there would be in an actual plasma, the

439 statistical uncertainties in our simulated currents are larger than those that would oc-
 440 cur in space under similar conditions. The tolerance of our models to statistical noise
 441 is assessed by adding varying levels of normally distributed noise to the currents in our
 442 validation sets, in addition to the numerical simulation noise mentioned above. The skill
 443 of both RBF and neural network regressions decreases as noise is added, and it is esti-
 444 mated that an additional 2% relative noise leads only to approximately doubling in the
 445 uncertainty of model inferences in both cases.

446 Several approximations were made in the simulations used to construct our train-
 447 ing and validation sets. In particular, the presence of a satellite bus was not taken into
 448 account, which is justified if the flow meter is mounted on the ram face of a satellite, and
 449 the fact that satellites in low Earth orbit have supersonic ram velocities. The geomag-
 450 netic field was also neglected, which is justified by the fact that typical ion thermal ion
 451 gyro-radii is a factor 10 or more, larger than the size of the sensor. The neglect of so-
 452 lar illumination and photoelectron emission is valid when the satellite is on the night side
 453 of its orbit. When the satellite is sunlit, however, it would be possible for the negatively
 454 biased ring at the sensor aperture, to emit photoelectrons which, owing to the negative
 455 bias, would be repelled, and appear as collected positive current. Solar UVs could also
 456 enter the aperture and reach directly, or indirectly through multiple reflections, the pos-
 457 itively biased segments. This in turn would result in photoelectrons being emitted in-
 458 side the flow meter which, owing to the positive bias of the segments at the base, would
 459 likely be attracted back to the segments, albeit, not necessarily at the exact position where
 460 they were emitted. This, and the exposition of the positive ring at the aperture, would
 461 likely affect measured currents, and require corrections in the models presented above
 462 to infer plasma parameters. These effects should be included in models constructed to
 463 support missions, in which specific spacecraft geometry, orbital parameters, and expected
 464 range of plasma environment parameters would be taken into account. Such an analy-
 465 sis is of course well beyond the scope of this preliminary study, as it would require ac-
 466 counting for a broader range of parameters and environmental conditions, and would re-
 467 quire significantly more simulations. Considering the investment and years of prepara-
 468 tion preceding a launch, such an investment, enabling better data acquisition, should nonethe-
 469 less be well justified.

470 Acknowledgments

471 This work was supported by the China Scholarship Council (CSC) and the Natural Sci-
 472 ences and Engineering Research Council of Canada. The kinetic simulations used in this
 473 study were made on the Compute Canada computing infrastructure. Simulation data
 474 can be accessed through https://zenodo.org/record/4434879#.X_4BAdhKhPZ (Liu,
 475 2021).

476 References

- 477 Baker, D. (2000). The occurrence of operational anomalies in spacecraft and their
 478 relationship to space weather. *IEEE Transactions on Plasma Science*, *28*(6),
 479 2007–2016. Retrieved from <http://ieeexplore.ieee.org/document/902228/>
 480 doi: 10.1109/27.902228
- 481 Barkhatov, N. A., & Revunov, S. E. (2010, dec). Neural network classification
 482 of discontinuities in space plasma parameters. *Geomagnetism and Aeron-*
 483 *omy*, *50*(7), 894–904. Retrieved from [http://link.springer.com/10.1134/](http://link.springer.com/10.1134/S001679321007011X)
 484 [S001679321007011X](http://link.springer.com/10.1134/S001679321007011X) doi: 10.1134/S001679321007011X
- 485 Berthelier, J., Godefroy, M., Leblanc, F., Malingre, M., Menvielle, M., Lagoutte,
 486 D., . . . Pfaff, R. (2006, apr). ICE, the electric field experiment on DEME-
 487 TER. *Planetary and Space Science*, *54*(5), 456–471. Retrieved from
 488 <https://linkinghub.elsevier.com/retrieve/pii/S0032063305002072>
 489 doi: 10.1016/j.pss.2005.10.016

- 490 Berthelier, J., Godefroy, M., Leblanc, F., Seran, E., Peschard, D., Gilbert, P.,
 491 & Artru, J. (2006, apr). IAP, the thermal plasma analyzer on DEME-
 492 TER. *Planetary and Space Science*, 54(5), 487–501. Retrieved from
 493 <https://linkinghub.elsevier.com/retrieve/pii/S0032063305002096>
 494 doi: 10.1016/j.pss.2005.10.018
- 495 Bilitza, D., Altadill, D., Zhang, Y., Mertens, C., Truhlik, V., Richards, P., ...
 496 Reinisch, B. (2014, feb). The International Reference Ionosphere 2012 – a
 497 model of international collaboration. *Journal of Space Weather and Space*
 498 *Climate*, 4, A07. Retrieved from [http://www.swsc-journal.org/10.1051/](http://www.swsc-journal.org/10.1051/swsc/2014004)
 499 [swsc/2014004](http://www.swsc-journal.org/10.1051/swsc/2014004) doi: 10.1051/swsc/2014004
- 500 Breuillard, H., Dupuis, R., Retino, A., Le Contel, O., Amaya, J., & Lapenta, G.
 501 (2020, sep). Automatic Classification of Plasma Regions in Near-Earth
 502 Space With Supervised Machine Learning: Application to Magnetospheric
 503 Multi Scale 2016–2019 Observations. *Frontiers in Astronomy and Space Sci-*
 504 *ences*, 7. Retrieved from [https://www.frontiersin.org/article/10.3389/](https://www.frontiersin.org/article/10.3389/fspas.2020.00055/full)
 505 [fspas.2020.00055/full](https://www.frontiersin.org/article/10.3389/fspas.2020.00055/full) doi: 10.3389/fspas.2020.00055
- 506 Buhmann, M. D. (2003). *Radial basis functions: theory and implementations*
 507 (Vol. 12). Cambridge university press.
- 508 Carlson, C., Curtis, D., Paschmann, G., & Michel, W. (1982, jan). An in-
 509 strument for rapidly measuring plasma distribution functions with high
 510 resolution. *Advances in Space Research*, 2(7), 67–70. Retrieved from
 511 <https://linkinghub.elsevier.com/retrieve/pii/027311778290151X>
 512 doi: 10.1016/0273-1177(82)90151-X
- 513 Carlson, C. W., & McFadden, J. P. (2013, mar). Design and Application of Imag-
 514 ing Plasma Instruments. In *Geophysical monograph series* (Vol. 102, pp. 125–
 515 140). Retrieved from <http://doi.wiley.com/10.1029/GM102p0125> doi: 10
 516 .1029/GM102p0125
- 517 Carlson, C. W., Mcfadden, J. P., Turin, P., Curtis, D. W., & Magoncelli, A. (2001).
 518 The electron and ion plasma experiment for FAST. *Space Science Reviews*,
 519 98(1-2), 33–66. doi: 10.1023/A:1013139910140
- 520 Davies, J. B., & Archambeau, C. B. (1998, jan). Modeling of atmospheric
 521 and ionospheric disturbances from shallow seismic sources. *Physics of*
 522 *the Earth and Planetary Interiors*, 105(3-4), 183–199. Retrieved from
 523 <https://linkinghub.elsevier.com/retrieve/pii/S0031920197000903>
 524 doi: 10.1016/S0031-9201(97)00090-3
- 525 De Santis, A., Marchetti, D., Pavón-Carrasco, F. J., Cianchini, G., Perrone, L.,
 526 Abbattista, C., ... Haagmans, R. (2019, dec). Precursory worldwide sig-
 527 natures of earthquake occurrences on Swarm satellite data. *Scientific Re-*
 528 *ports*, 9(1), 20287. Retrieved from [http://www.nature.com/articles/](http://www.nature.com/articles/s41598-019-56599-1)
 529 [s41598-019-56599-1](http://www.nature.com/articles/s41598-019-56599-1) doi: 10.1038/s41598-019-56599-1
- 530 Englert, C. R., Babcock, D. D., & Harlander, J. M. (2007, oct). Doppler
 531 asymmetric spatial heterodyne spectroscopy (DASH): concept and exper-
 532 imental demonstration. *Applied Optics*, 46(29), 7297. Retrieved from
 533 <https://www.osapublishing.org/abstract.cfm?URI=ao-46-29-7297> doi:
 534 10.1364/AO.46.007297
- 535 Ergun, R. E., Carlson, C. W., Mozer, F. S., Delory, G. T., Temerin, M., Mcfadden,
 536 J. P., ... Cattell, C. A. (2001). The fast satellite fields instrument. *Space*
 537 *Science Reviews*, 98(1-2), 67–91. doi: 10.1023/A:1013131708323
- 538 Frey, P., & George, P. L. (2007). *Mesh Generation: Application to Finite Elements*.
 539 London, UK: ISTE.
- 540 Galperin, Y., Ponomarev, V., & Zosimova, A. (1973, oct). *Direct measurements*
 541 *of ion drift velocity in the upper ionosphere during a magnetic storm. Part 1:*
 542 *Experiment description and some results of measurements during magnetically*
 543 *quiet time.*
- 544 Galperin, Y., Ponomarev, V. N., & Zosimova, A. G. (1974). Plasma convection in

- 545 polar ionosphere. *Annales de Geophysique*, 30(1), 1–7.
- 546 Geuzaine, C., & Remacle, J.-F. (2009, sep). Gmsh: A 3-D finite element mesh gener-
 547 ator with built-in pre- and post-processing facilities. *International Journal*
 548 *for Numerical Methods in Engineering*, 79(11), 1309–1331. Retrieved from
 549 <http://doi.wiley.com/10.1002/nme.2579> doi: 10.1002/nme.2579
- 550 Hanson, W. B., & Heelis, R. A. (1975, nov). Techniques for measuring bulk gas-
 551 motions from satellites. *Space Science Instrumentation*, 1, 493–524.
- 552 Hanson, W. B., Zuccaro, D. R., Lippincott, C. R., & Sanatani, S. (1973, apr). The
 553 retarding-potential analyzer on Atmosphere Explorer. *Radio Science*, 8(4),
 554 333–339. Retrieved from <http://doi.wiley.com/10.1029/RS008i004p00333>
 555 doi: 10.1029/RS008i004p00333
- 556 Heelis, R., Hanson, W., Lippincott, C., Zuccaro, D., Harmon, L., Holt, B., ...
 557 Power, R. (1981, dec). The Ion Drift Meter for Dynamics Explorer-B. *Space*
 558 *Science Instrumentation*, 5, 511–521.
- 559 Heelis, R. A., & Hanson, W. B. (2013, mar). Measurements of Thermal Ion Drift
 560 Velocity and Temperature Using Planar Sensors. In *Geophysical mono-*
 561 *graph series* (Vol. 102, pp. 61–71). American Geophysical Union (AGU).
 562 Retrieved from [https://agupubs.onlinelibrary.wiley.com/doi/abs/](https://agupubs.onlinelibrary.wiley.com/doi/abs/10.1029/GM102p0061)
 563 [10.1029/GM102p0061](http://doi.wiley.com/10.1029/GM102p0061)<http://doi.wiley.com/10.1029/GM102p0061> doi:
 564 10.1029/GM102p0061
- 565 Heelis, R. A., Stoneback, R. A., Perdue, M. D., Depew, M. D., Morgan, W. A.,
 566 Mankey, M. W., ... Holt, B. J. (2017, oct). Ion Velocity Measurements for the
 567 Ionospheric Connections Explorer. *Space Science Reviews*, 212(1-2), 615–629.
 568 doi: 10.1007/s11214-017-0383-3
- 569 Hundhausen, A. J., Asbridge, J. R., Bame, S. J., Gilbert, H. E., & Strong, I. B.
 570 (1967). Vela 3 satellite observations of solar wind ions: A preliminary re-
 571 port. *Journal of Geophysical Research*, 72(1), 87. Retrieved from [http://](http://doi.wiley.com/10.1029/JZ072i001p00087)
 572 doi.wiley.com/10.1029/JZ072i001p00087 doi: 10.1029/JZ072i001p00087
- 573 Knudsen, D. J., Burchill, J. K., Berg, K., Cameron, T., Enno, G. A., Marcellus,
 574 C. G., ... King, R. A. (2003, jan). A low-energy charged particle distribution
 575 imager with a compact sensor for space applications. *Review of Scientific In-*
 576 *struments*, 74(1), 202–211. Retrieved from [http://aip.scitation.org/doi/](http://aip.scitation.org/doi/10.1063/1.1525869)
 577 [10.1063/1.1525869](http://aip.scitation.org/doi/10.1063/1.1525869) doi: 10.1063/1.1525869
- 578 Knudsen, D. J., Burchill, J. K., Buchert, S. C., Eriksson, A. I., Gill, R., Wahlund,
 579 J., ... Moffat, B. (2017, feb). Thermal ion imagers and Langmuir probes in
 580 the Swarm electric field instruments. *Journal of Geophysical Research: Space*
 581 *Physics*, 122(2), 2655–2673. Retrieved from [https://onlinelibrary.wiley](https://onlinelibrary.wiley.com/doi/abs/10.1002/2016JA022571)
 582 [.com/doi/abs/10.1002/2016JA022571](https://onlinelibrary.wiley.com/doi/abs/10.1002/2016JA022571) doi: 10.1002/2016JA022571
- 583 Krasnov, V., & Drobzheva, Y. (2005, jul). The acoustic field in the iono-
 584 sphere caused by an underground nuclear explosion. *Journal of Atmo-*
 585 *spheric and Solar-Terrestrial Physics*, 67(10), 913–920. Retrieved from
 586 <https://linkinghub.elsevier.com/retrieve/pii/S1364682605000647>
 587 doi: 10.1016/j.jastp.2005.02.014
- 588 Lebreton, J.-P., Stverak, S., Travnicsek, P., Maksimovic, M., Klinge, D., Merikallio,
 589 S., ... Salaquarda, M. (2006, apr). The ISL Langmuir probe experiment
 590 processing onboard DEMETER: Scientific objectives, description and first
 591 results. *Planetary and Space Science*, 54(5), 472–486. Retrieved from
 592 <https://linkinghub.elsevier.com/retrieve/pii/S0032063305002084>
 593 doi: 10.1016/j.pss.2005.10.017
- 594 Liu, G. (2021, jan). *Segmented flow meter data*. Zenodo. Retrieved from [https://](https://doi.org/10.5281/zenodo.4434879)
 595 doi.org/10.5281/zenodo.4434879 doi: 10.5281/zenodo.4434879
- 596 Marchand, R. (2012, feb). PTetra, a Tool to Simulate Low Orbit Satellite–Plasma
 597 Interaction. *IEEE Transactions on Plasma Science*, 40(2), 217–229. Retrieved
 598 from <http://ieeexplore.ieee.org/document/6069605/> doi: 10.1109/TPS
 599 .2011.2172638

- 600 Marchand, R., Burchill, J. K., & Knudsen, D. J. (2010, oct). Modelling Electrostatic
601 Sheath Effects on Swarm Electric Field Instrument Measurements. *Space Sci-*
602 *ence Reviews*, 156(1-4), 73–87. Retrieved from [http://link.springer.com/](http://link.springer.com/10.1007/s11214-010-9735-y)
603 [10.1007/s11214-010-9735-y](http://link.springer.com/10.1007/s11214-010-9735-y) doi: 10.1007/s11214-010-9735-y
- 604 Marchand, R., & Resendiz Lira, P. A. (2017, apr). Kinetic Simulation of Space-
605 craft–Environment Interaction. *IEEE Transactions on Plasma Science*, 45(4),
606 535–554. Retrieved from <http://ieeexplore.ieee.org/document/7888602/>
607 doi: 10.1109/TPS.2017.2682229
- 608 Ogilvie, K. W., Chornay, D. J., Fritzenreiter, R. J., Hunsaker, F., Keller, J., Lo-
609 bell, J., ... Gergin, E. (1995, feb). SWE, a comprehensive plasma instru-
610 ment for the WIND spacecraft. *Space Science Reviews*, 71(1-4), 55–77.
611 Retrieved from <http://link.springer.com/10.1007/BF00751326> doi:
612 10.1007/BF00751326
- 613 Parrot, M. (2012, apr). Statistical analysis of automatically detected ion den-
614 sity variations recorded by DEMETER and their relation to seismic ac-
615 tivity. *Annals of Geophysics*, 55(1), 149–155. Retrieved from [https://](https://www.annalsofgeophysics.eu/index.php/annals/article/view/5270)
616 www.annalsofgeophysics.eu/index.php/annals/article/view/5270 doi:
617 10.4401/ag-5270
- 618 Parrot, M., Berthelier, J., Lebreton, J., Sauvaud, J., Santolik, O., & Blecki,
619 J. (2006, jan). Examples of unusual ionospheric observations made
620 by the DEMETER satellite over seismic regions. *Physics and Chem-*
621 *istry of the Earth, Parts A/B/C*, 31(4-9), 486–495. Retrieved from
622 <https://linkinghub.elsevier.com/retrieve/pii/S147470650600043X>
623 doi: 10.1016/j.pce.2006.02.011
- 624 Pirjola, R. (2000). Geomagnetically induced currents during magnetic storms. *IEEE*
625 *Transactions on Plasma Science*, 28(6), 1867–1873. doi: 10.1109/27.902215
- 626 Reigber, C., Lühr, H., & Schwintzer, P. (Eds.). (2003). *First CHAMP Mission*
627 *Results for Gravity, Magnetic and Atmospheric Studies*. Berlin, Heidelberg:
628 Springer Berlin Heidelberg. Retrieved from [http://link.springer.com/](http://link.springer.com/10.1007/978-3-540-38366-6)
629 [10.1007/978-3-540-38366-6](http://link.springer.com/10.1007/978-3-540-38366-6) doi: 10.1007/978-3-540-38366-6
- 630 Rudenko, G., & Uralov, A. (1995, mar). Calculation of ionospheric effects due
631 to acoustic radiation from an underground nuclear explosion. *Journal*
632 *of Atmospheric and Terrestrial Physics*, 57(3), 225–236. Retrieved from
633 <https://linkinghub.elsevier.com/retrieve/pii/0021916993E0003R> doi:
634 10.1016/0021-9169(93)E0003-R
- 635 Ryu, K., Lee, E., Chae, J. S., Parrot, M., & Pulinets, S. (2014, oct). Seismo-
636 ionospheric coupling appearing as equatorial electron density enhancements
637 observed via DEMETER electron density measurements. *Journal of Geophys-*
638 *ical Research: Space Physics*, 119(10), 8524–8542. Retrieved from [http://](http://doi.wiley.com/10.1002/2014JA020284)
639 doi.wiley.com/10.1002/2014JA020284 doi: 10.1002/2014JA020284
- 640 Saad, Y. (2003). *Iterative Methods for Sparse Linear Systems* (Second ed.). Society
641 for Industrial and Applied Mathematics. Retrieved from [https://epubs.siam](https://epubs.siam.org/doi/abs/10.1137/1.9780898718003)
642 [.org/doi/abs/10.1137/1.9780898718003](https://epubs.siam.org/doi/abs/10.1137/1.9780898718003)[http://epubs.siam.org/doi/](http://epubs.siam.org/doi/book/10.1137/1.9780898718003)
643 [book/10.1137/1.9780898718003](http://epubs.siam.org/doi/book/10.1137/1.9780898718003) doi: 10.1137/1.9780898718003
- 644 Sangalli, L., Knudsen, D. J., Larsen, M. F., Zhan, T., Pfaff, R. F., & Rowland,
645 D. (2009, apr). Rocket-based measurements of ion velocity, neutral wind,
646 and electric field in the collisional transition region of the auroral iono-
647 sphere. *Journal of Geophysical Research: Space Physics*, 114(A4), n/a–
648 n/a. Retrieved from <http://doi.wiley.com/10.1029/2008JA013757> doi:
649 10.1029/2008JA013757
- 650 Santandrea, S., Gantois, K., Strauch, K., Teston, F., Tilmans, E., Baijot, C., ...
651 Zender, J. (2013, aug). PROBA2: Mission and Spacecraft Overview. *Solar*
652 *Physics*, 286(1), 5–19. Retrieved from [http://link.springer.com/10.1007/](http://link.springer.com/10.1007/s11207-013-0289-5)
653 [s11207-013-0289-5](http://link.springer.com/10.1007/s11207-013-0289-5) doi: 10.1007/s11207-013-0289-5
- 654 Satir, M., Sik, F., Turkoz, E., & Celik, M. (2015, jun). Design of the retard-

- 655 ing potential analyzer to be used with BURFIT-80 Ion thruster and val-
 656 idation using PIC-DSMC code. In *2015 7th international conference on*
 657 *recent advances in space technologies (rast)* (pp. 577–582). IEEE. Re-
 658 trieved from <http://ieeexplore.ieee.org/document/7208410/> doi:
 659 10.1109/RAST.2015.7208410
- 660 Séran, E. (2003). Reconstruction of the ion plasma parameters from the cur-
 661 rent measurements: Mathematical tool. *Annales Geophysicae*, *21*(5), 1159–
 662 1166. Retrieved from <http://www.ann-geophys.net/21/1159/2003/> doi:
 663 10.5194/angeo-21-1159-2003
- 664 Séran, E., Berthelier, J.-J., Saouri, F. Z., & Lebreton, J.-P. (2005, jul). The spher-
 665 ical segmented Langmuir probe in a flowing thermal plasma: numerical model
 666 of the current collection. *Annales Geophysicae*, *23*(5), 1723–1733. Retrieved
 667 from <https://angeo.copernicus.org/articles/23/1723/2005/> doi:
 668 10.5194/angeo-23-1723-2005
- 669 Shen, X. H., Zhang, X. M., Yuan, S. G., Wang, L. W., Cao, J. B., Huang, J. P.,
 670 ... Dai, J. P. (2018, may). The state-of-the-art of the China Seismo-
 671 Electromagnetic Satellite mission. *Science China Technological Sciences*,
 672 *61*(5), 634–642. Retrieved from [http://link.springer.com/10.1007/](http://link.springer.com/10.1007/s11431-018-9242-0)
 673 [s11431-018-9242-0](http://link.springer.com/10.1007/s11431-018-9242-0) doi: 10.1007/s11431-018-9242-0
- 674 Stoneback, R. A., Davidson, R. L., & Heelis, R. A. (2012, aug). Ion drift
 675 meter calibration and photoemission correction for the C/NOFS satel-
 676 lite. *Journal of Geophysical Research: Space Physics*, *117*(A8), n/a–n/a.
 677 Retrieved from <http://doi.wiley.com/10.1029/2012JA017636> doi:
 678 10.1029/2012JA017636
- 679 Whalen, B. A., Knudsen, D. J., Yau, A. W., Pilon, A. M., Cameron, T. A., Sebesta,
 680 J. F., ... Campbell, G. S. (1994, nov). The Freja F3C Cold Plasma Ana-
 681 lyzer. *Space Science Reviews*, *70*(3-4), 541–561. Retrieved from [http://](http://link.springer.com/10.1007/BF00756885)
 682 link.springer.com/10.1007/BF00756885 doi: 10.1007/BF00756885
- 683 Yang, Y.-M., Garrison, J. L., & Lee, S.-C. (2012, jan). Ionospheric distur-
 684 bances observed coincident with the 2006 and 2009 North Korean un-
 685 derground nuclear tests. *Geophysical Research Letters*, *39*(2), n/a–n/a.
 686 Retrieved from <http://doi.wiley.com/10.1029/2011GL050428> doi:
 687 10.1029/2011GL050428
- 688 Yau, A. W., Garbe, G. P., Greffen, M. J., Miyake, W., & Sagawa, E. (1998, mar).
 689 Planned observations of thermal plasma drifts and solar wind interactions in
 690 the Martian ionosphere. *Earth, Planets and Space*, *50*(3), 195–198. Retrieved
 691 from [http://earth-planets-space.springeropen.com/articles/10.1186/](http://earth-planets-space.springeropen.com/articles/10.1186/BF03352103)
 692 [BF03352103](http://earth-planets-space.springeropen.com/articles/10.1186/BF03352103) doi: 10.1186/BF03352103
- 693 Yau, A. W., Howarth, A., White, A., Enno, G., & Amerl, P. (2015). Imaging and
 694 Rapid-Scanning Ion Mass Spectrometer (IRM) for the CASSIOPE e-POP
 695 Mission. *Space Science Reviews*, *189*(1-4), 41–63. Retrieved from [http://](http://dx.doi.org/10.1007/s11214-015-0149-8)
 696 dx.doi.org/10.1007/s11214-015-0149-8 doi: 10.1007/s11214-015-0149-8